Results from a double Li-beam technique for measurement of both radial and poloidal components of electron density fluctuations using two thermal beams

View the table of contents for this issue, or go to the journal homepage for more

Results from a double Li-beam technique for measurement of both radial and poloidal components of electron density fluctuations using two thermal beams

A Huber, U Samm, B Schweer and Ph Mertens

Institut für Plasmaphysik, Forschungszentrum Jülich GmbH, EURATOM Association, Trilateral Euregio Cluster, D-52425 Jülich, Germany

E-mail: A.Huber@fz-juelich.de

Abstract

Determination of both the radial and poloidal components of electron density fluctuation parameters in a tokamak edge plasma was achieved by operation of two narrow Li-beams (FWHM $\approx$10 mm at a distance of 100 mm from the source), which were separated by 50 mm. Beams of thermal lithium atoms were generated using a newly developed oven, which provides a long operation time and a high reliability. The lithium atoms, with a mean velocity of $\approx$1.7 km s^{-1}, were injected radially into the plasma edge, where they were excited and ionized by the plasma. The line radiation (resonance transition 2s–2p, λ = 670.8 nm) of the excited atoms was observed, which enables determination of the electron density profiles. The measurements are performed with high temporal ($\Delta t \simeq 2\,\mu$s) and spatial ($\Delta_r \simeq 1$ mm in the radial and $\Delta_p \simeq 10$ mm in the poloidal direction) resolution, thus also allowing determination of the fluctuations. This new diagnostic permits studies of both radial and poloidal fluctuation parameters like the correlation length, wavenumber, frequency spectrum, propagation velocity and lifetime. The method can be applied continuously over long discharges without disturbing the plasma.

(Some figures in this article are in colour only in the electronic version)

1. Introduction

Turbulent fluctuations are the most probable indication of anomalous transport of energy and particles in tokamaks. But the mechanisms responsible for these instabilities are not yet fully understood. An improved knowledge of the spatio-temporal structure of fluctuations is a prerequisite for a deeper comprehension. In particular, information about the spatial structure

of the fluctuations in the radial and poloidal directions in the scrape-off layer (SOL) would help study transport mechanisms at the plasma boundary.

Turbulent plasma fluctuations were the object of intensive investigations in many tokamaks for many years (see, e.g. [1,5] and the reviews [2–4]). However, despite numerous experimental data, this information is not enough for an actual understanding of the measurements in terms of the basic theory of edge plasma turbulence. Additionally, the measurements of fluctuation structures were mostly performed by means of multichannel measurements based on Langmuir probes [6] and with beam emission spectroscopy (e.g. diagnostics with a highly energetic Li-beam [7]). The study of the fluctuations with radial resolution using Langmuir probes is problematic, since the probe pins disturb the plasma. In the case of beam emission spectroscopy, the velocity, v, of the injected atoms limits the spatial resolution of the measurements (see section 3).

In the past few years, the theory of edge plasma turbulence has advanced rapidly [8–11]. Therefore, for comparison of experiment and theory, the most interesting turbulent structure is in the radial versus poloidal plane, i.e. perpendicular to the total magnetic field. The first two-dimensional images of edge turbulence were obtained as early as 1985, using 64-point Langmuir probe arrays [1]. In the past few years, two-dimensional turbulence structures were investigated by means of a 32-point two-dimensional array of beam emission spectroscopy [12] and using edge turbulence imaging systems [13].

A new technique using spectroscopic observations of thermal atomic beams for measurement of the electron density fluctuation in the SOL and a few centimetres further inside the last closed flux surface (LCFS) was developed, tested and applied on the TEXTOR tokamak. This new diagnostic allows measurements of both radial and poloidal fluctuation parameters like correlation lengths, the wavenumber, the frequency spectrum, the propagation velocity and the lifetime. The advantage of this method in comparison with Langmuir probes is the good spatial and temporal resolution, which can be achieved without disturbing the plasma. Moreover, the use of continuous beams makes measurements possible during the entire discharge. However, only measurement of electron density fluctuations is possible with this method. Resolving the fluctuations in both the radial and poloidal directions is of particular importance. The aim of this work is the development, application and testing of a spectroscopic method for measurement of the electron density fluctuations. The method ought to meet the following requirements:

- the Li-beam should not influence the plasma parameters;
- the fluctuations should be measured with sufficient spatial resolution in both the radial and poloidal directions;
- the method should have sufficient temporal resolution on top, to allow determination of n_e and $\tilde{n}_e$ simultaneously.

This paper is organized as follows: in section 2 we present the basic physics concepts of emission spectroscopy that are of importance for experiments with the Li-beam diagnostic. Here, the principles of measurement for determination of the electron density profiles and its fluctuations are also presented. Using the collisional–radiative model, we discuss in section 3 relaxation times and their importance for fluctuation measurements with beam diagnostics. In section 4, we describe the experimental arrangement of the Li-beam diagnostic at TEXTOR. The details of the Li-source developed specifically for these measurements are explained. Section 5 presents the technique used to identify the poloidal separation between the beams. The limits of the diagnostic are discussed in section 6, in which selected measurements on TEXTOR are presented and discussed. Furthermore, the influence of the beam width on the spectra and on the poloidal correlation functions is presented.

2. Principles of the Li-beam diagnostic

The method is based on the interaction of thermal neutral lithium atoms with the plasma. Li-atoms are injected into the plasma with a thermal velocity of $\upsilon \approx 1.7\,\mathrm{km\,s^{-1}}$. They are excited from the ground state by electron impact. Excited atomic states decay spontaneously. The number of transitions per unit time gives the photon flux. A local profile of the electron density can be deduced from the radial line emission profile.

2.1. Basic physical concept

The coupling of the emitted intensity with the electron density, the fluctuations of which are the subject of investigation, has to be described. The intensity of the line radiation of optically thin plasmas can be obtained from the emission coefficient (radiation efficiency per volume and solid angle):

$$\epsilon_{ij} = \frac{h\nu_{ij}}{4\pi} n_i A_{ij}, \tag{1}$$

where n_i is the population density in an excited state i with transition probability A_{ij} for spontaneous emission from an upper state i to lower state j. The frequency and the energy of the transition are represented by ν_{ij} and $\Delta E_{ij} = h\nu_{ij}$. The emission coefficient has the units $\mathrm{W\,m^{-3}\,sr^{-1}}$. Integration along the line of sight crossing the beam determines the measured intensity, I ($\mathrm{W\,m^{-2}\,sr^{-1}}$).

$$I = \frac{1}{4\pi} \int h\nu_{ij} n_i A_{ij}\,\mathrm{d}l. \tag{2}$$

At a low electron density, the population densities of the excited states are very small and the injected atoms, n_0, are mainly in the ground state, n_1 ($n_1 \approx n_0$ and $n_i \ll n_1$). As a consequence, higher states are populated by single electron collisions and are subsequently depopulated into lower states by radiative transitions only. De-excitation by impact processes can be neglected.

$$n_i A_{ij} \gg n_e n_i \langle \sigma \upsilon_e \rangle_{\mathrm{el.impact}}, \tag{3}$$

where $\langle \sigma \upsilon_e \rangle_{\mathrm{el.impact}}$ are the rate coefficients for decay upon electron impact. This is the so-called *corona model* [14]. In this case, the change in population density, n_i, of the state i is described by

$$\frac{\mathrm{d}n_i}{\mathrm{d}t} = n_e n_1 \langle \sigma_{\mathrm{Ex}} \upsilon_e \rangle - \sum_{j<i} n_i A_{ij}. \tag{4}$$

Here, $\langle \sigma_{\mathrm{Ex}} \upsilon_e \rangle$ represents the excitation rate coefficient for electron impact from the ground state, and n_1 the population density of the ground state. In the stationary case, the population density of state i is given by

$$n_i = n_e n_1 \frac{\langle \sigma_{\mathrm{Ex}} \upsilon_e \rangle}{\sum_{j<i} A_{ij}}. \tag{5}$$

Therefore, the measured intensity, I, is directly proportional to the product of the ground state and electron density:

$$I = \frac{h\nu_{ij}}{4\pi} \frac{A_{ij}}{\sum_{j<i} A_{ij}} n_1 n_e \langle \sigma_{\mathrm{Ex}} \upsilon_e \rangle \cdot d, \tag{6}$$

where d is the diameter of the neutral particle beam. The ratio $A_{ij} / \sum_{j<i} A_{ij}$ is the branching ratio for the line emission observed. Since in equation (6) the electron density, n_e, is the only

fast fluctuating parameter, the intensity of fluctuations, $\tilde{I}$, is proportional to the electron density fluctuation, $\tilde{n}_e$, and the following assumption is valid:

$$\frac{\tilde{I}}{I} = \frac{\tilde{n}_e}{n_e}. \tag{7}$$

The deviation from this relation by the neutral particle fluctuations $\tilde{n}_1(t)$ is analysed in detail in [15]. If the beam attenuation is only caused by electron collisions, the neutral particle density, $n_0(r)$, may be described with the following differential equation:

$$\frac{\partial n_0(v,r,t)}{\partial t} + v\frac{\partial n_0(v,r,t)}{\partial r} = -\langle \sigma_I v_e \rangle n_e(r,t) n_0(v,r,t). \tag{8}$$

Here $\langle \sigma_I v_e \rangle$ is the rate coefficient for ionization by electron collision and $n_e(r)$ the electron density at the position r. If the neutral particle density, n_0, is time independent and the atoms leave the source with a narrow velocity distribution, $f(v)$, this equation can be simplified as

$$\frac{\partial n_0(r)}{\partial r} = -n_e(r)n_0(r)\frac{\langle \sigma_I v_e \rangle}{\bar{v}}, \tag{9}$$

where $\bar{v} = \int vf(v)\mathrm{d}v / \int f(v)\mathrm{d}v$ is the mean velocity of the beam. The neutral particle density, $n_0(r)$, at distance a from the source, can be obtained by integration:

$$n_0(a) = -\int_a^{\infty} n_e(r')n_0(r')\frac{\langle \sigma_I v_e \rangle}{\bar{v}}\,\mathrm{d}r'. \tag{10}$$

For application in a tokamak, it is reasonable to select the minor plasma radius as a reference system. The beam is directed to the plasma centre ($r = 0$). The integration limits run from 0 to r:

$$n_0(r) = \int_0^r n_e(r')n_0(r')\frac{\langle \sigma_I v_e \rangle}{\bar{v}}\,\mathrm{d}r'. \tag{11}$$

Therefore, the attenuation of the atomic beam depends on the electron density, on the rate coefficient for ionization (this is where the dependence on electron temperature might come in) and on the mean beam velocity. It is assumed that all neutral particles are ionized before reaching the plasma centre.

2.2. Selection of a suitable spectral line

If the rate coefficient for excitation by electron impact $\langle \sigma_{Ex} v_e \rangle$ from the ground state into state i is independent of the electron temperature, the local electron density can be determined from the spectral line intensity. In this case, the depopulation of the ground state should also be temperature independent, i.e. $\langle \sigma_I v_e \rangle \neq f(T_e)$. It is very important for the selection of the spectral line to consider that the emission coefficient should be as large as possible. In figure 1, the energy level diagram of Li up to the main quantum number $n = 3$ is presented. The transition 2p–2s with emission at $\lambda = 670.8$ nm was selected, which offers the following advantages:

- The rate coefficient for the excitation process by electron collision from the ground state into the state 2p is large $\langle \sigma_{2s-2p} v_e \rangle \approx 8 \times 10^{-13}\,\mathrm{m^3\,s^{-1}}$ (see figure 2). It is more than a factor of 10 larger than for the states 3s, 3p and 3d ($\langle \sigma v_e \rangle = 1.5 \times 10^{-14}\,\mathrm{m^3\,s^{-1}}$ and $4 \times 10^{-14}\,\mathrm{m^3\,s^{-1}}$, respectively). About 2.3% of the Li-atoms are in the 2p-state at an electron density of $1 \times 10^{18}\,\mathrm{m^{-3}}$. That is clearly more than in the states 3s, 3p and 3d with 0.075%, 0.13% and 0.09%, respectively.
- The rate coefficients for electron impact excitation and ionization vary only weakly in the temperature range between 10 and 100 eV (figure 2).
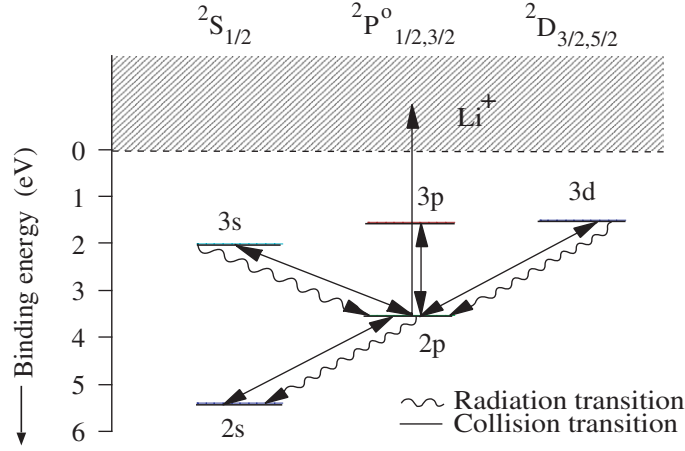
Figure 1. Term diagram of the lithium atom, represented up to the principal quantum number $n = 3$.
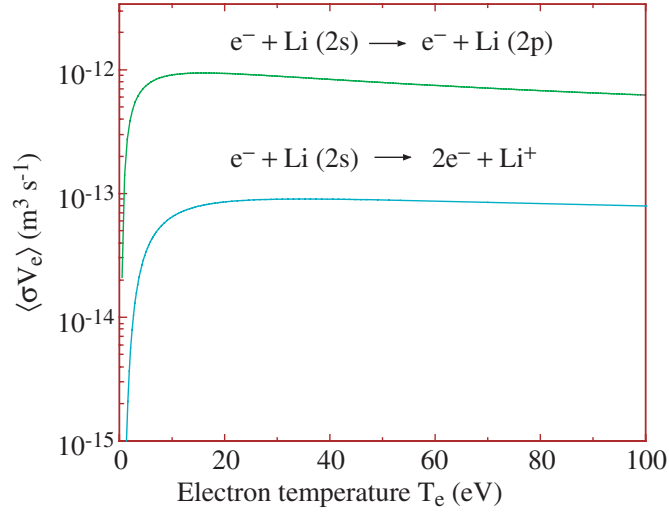
Figure 2. Rate coefficient for electron impact ionization of the ground state and for electron impact excitation from the ground state, 2s, to the 2p state.

- For determination of the electron density, only two states are considered: the ground state, 2s, and the state 2p.
- The depopulation of the 2p-state only occurs by a radiative transition (2p–2s). The branching ratio is $A_{ij} / \sum_{j<i} A_{ij} = 1$.

2.3. Reconstruction of electron density profiles

If a neutral particle beam of lithium atoms is injected into a plasma, the penetration depth of these particles is determined by ionization processes only. In the electron temperature range between 10 and 100 eV, typical for edge plasmas in a tokamak, the attenuation depends only on

Table 1. Comparison of some collisional rates for electron and proton impact processes with lithium in the ground state ($n_e = 10^{18}$ m^{-3}, $T_e = 50$ eV).

Process	0.06 eV (thermal)	1 keV	10 keV
Excitation through e impact			
$e + Li(2s) \rightarrow e + Li(2p)$	8.0×10^5 s^{-1}	8.0×10^5 s^{-1}	8.0×10^5 s^{-1}
Ionization through e impact			
$e + Li(2s) \rightarrow 2e + Li^+$	9.0×10^4 s^{-1}	9.0×10^4 s^{-1}	9.0×10^4 s^{-1}
Excitation through p impact			
$p + Li(2s) \rightarrow p + Li(2p)$	$<10^4$ s^{-1}	1.5×10^4 s^{-1}	1.4×10^5 s^{-1}
Ionization through p impact			
$p + Li(2s) \rightarrow p + e + Li^+$	$<10^4$ s^{-1}	$\approx 2 \times 10^4$ s^{-1}	1.5×10^5 s^{-1}
p charge exchange			
$p + Li(2s) \rightarrow H + Li^+$	$<3 \times 10^3$ s^{-1}	5.0×10^3 s^{-1}	1.05×10^5 s^{-1}

the electron density. Based upon the measurement of the radial intensity profile of the spectral line emission, $I(r)$, the radial profile of the electron density can be derived by combining equations (11) and (6) [16–19], assuming $n_1(r) \approx n_0(r)$:

$$n_e(r) = \frac{\bar{v} I(r)}{\langle \sigma_{Ex} v_e \rangle \int_0^r (\langle \sigma_I v_e \rangle / \langle \sigma_{Ex} v_e \rangle) I(r') dr'}. \tag{12}$$

Since the ratio $\langle \sigma_I v_e \rangle / \langle \sigma_{Ex} v_e \rangle$ can be considered constant in the temperature range considered (10–100 eV), equation (12) can be simplified to

$$n_e(r) = \frac{\bar{v} I(r)}{\langle \sigma_I v_e \rangle \int_0^r I(r') dr'}. \tag{13}$$

The evaluation of the electron density requires no absolute calibration of I and is independent of the neutral particle flux. An essential requirement is that the full radial emission profile has to be considered.

The radial range of the measurement is defined by the penetration depth, ℓ, of the Li-atoms into the plasma edge, arbitrarily defined as the length corresponding to a decrease in the Li-flux by a factor of 10—which corresponds to our detection limit. It depends on the electron density, $n_e(x)$, the velocity, v, of the atoms and the rate coefficient, $\langle \sigma_I v_e \rangle$, for the ionization process.

$$\int_0^\ell n_e(x) dx = \frac{\bar{v}}{\langle \sigma_I v_e \rangle} \approx 4.3 \times 10^{16} \, \text{m}^{-2}. \tag{14}$$

Here, a typical oven temperature of 700°C was assumed. Taking the profile of typical TEXTOR ohmic discharges with a line-averaged electron density of 1.5×10^{19} m^{-3}, the penetration depth corresponds to a radius of $r = 430$ mm.

2.4. Influence of protons and of impurities on the density determination

For evaluation of the electron density, it was assumed that the collisions with protons can be neglected. The contributions of different impact processes in plasmas which can lead to an excitation and ionization of lithium-atoms are given in table 1. It can be seen from these values that excitation and ionization by protons can be neglected for small beam energies only. Impact rates are tabulated for electron collisions, for proton impacts and for charge exchange processes at a density of 10^{18} m^{-3} and an electron temperature of 50 eV. The rate coefficients used are taken from [20] and [21]. The columns of the table correspond to different kinetic energies of the lithium atoms. Collision rates $(n \cdot \langle \sigma v \rangle) < 10^4$ s^{-1} for electrons and $<3 \times 10^3$ s^{-1} for

protons are not considered further in these publications. We can see that impacts of fast Li-atoms with protons do not play a significant role below 1 keV. As shown in [22], the charge exchange cross-sections of Li with multiply charged impurity ions could be large. For example the maximum of the cross-section, σ_{max}, for the reaction $C^{6+} + Li(2s) \rightarrow C^{5+} + Li^+$ is about $10^{-18} \, m^2$. Carbon is chosen because it is one of the main low-Z impurities in TEXTOR. But, because of the small velocity of C^{6+} ions ($\upsilon_{C^{6+}} \approx 2.8 \times 10^4 \, m \, s^{-1}$ for $T_e = 50 \, eV$) and a low concentration of C-impurities in typical TEXTOR plasma conditions ($C/D \approx 0.03$ in the SOL), the contribution of such ions to the attenuation of the Li-beam via charge exchange is small. The charge exchange rate (approximately estimated as $\sigma_{max} \cdot \upsilon_{C^{6+}} \cdot n_{C^{6+}}$ for $n_e = 10^{18} \, m^{-3}$) is about $10^3 \, s^{-1}$ and is thus much smaller than the rates for excitation and ionization through electron impact. Impact processes of Li-atoms with impurities must be considered only in the case of fast Li-beams with injection energies $>10 \, keV$ [23].

3. Collisional–radiative model

For the study of fluctuations, it is important to answer the following questions. What is the maximal frequency that can be measured using the Li-beam technique? Is it possible to use the simple two-level-model without consideration of the upper levels and what is the influence of the upper levels on our measurements? The collisional–radiative model can give answers to these questions.

When Li-atoms are penetrating into the plasma, their density decreases due to ionization processes. However, the population density in a given volume reaches stationary conditions only after a certain relaxation time t_{rel}. All calculations for determination of the electron density profiles assume that the residence of the particles in the observation volume is longer than t_{rel}. The finite relaxation time has some consequences:

- An upper frequency limit for time resolved measurements is given by the relaxation time according to $f < 1/t_{rel}$.
- The local displacement of the excited atoms during the relaxation time must be smaller than the correlation length (L_r) of the fluctuations along the beam axis. As a consequence, the beam velocity, υ, must be smaller than the ratio $\upsilon < L_r/t_{rel}$.

The population densities for Li were computed up to the main quantum number $n = 4$. The following processes were considered in this model: ionization by electron collisions from all states; excitation and de-excitation impacts of electrons between the states; gains and losses in the population distribution by spontaneous emissions. One gets the following system of equations for calculation of the population densities $n_i(t)$ [$i = 1, \ldots, 9$] of the lithium atoms:

$$\frac{dn_i}{dt} = + \sum_{j \neq i} \langle \sigma \upsilon_e \rangle_{j \rightarrow i} n_e n_j \quad \text{(population by electron collisions from levels } j\text{)}$$

$$- \sum_{j \neq i} \langle \sigma \upsilon_e \rangle_{i \rightarrow j} n_e n_i \quad \text{(depopulation by electron collisions)}$$

$$+ \sum_{j > i} A_{ji} n_j - \sum_{j < i} A_{ij} n_i \quad \text{(gains and losses to the state } i \text{ by spontaneous emission)}$$

$$- \langle \sigma \upsilon_e \rangle_{i \rightarrow ion} n_e n_i \quad \text{(depopulation by ionization)}.$$

Here $\langle \sigma \upsilon_e \rangle_{j \rightarrow i}$ is the rate coefficient for electron-impact excitation from the state j to i, $\langle \sigma \upsilon_e \rangle_{i \rightarrow ion}$ the rate coefficient for electron-impact ionization from i into the continuum and A_{ij} the transition probability for spontaneous emission from i to j. The initial conditions of the population densities of the Li-atoms at $t = 0$ are set to $n_1|_{t=0} = n_0$; $n_i|_{t=0} = 0$, $i > 1$.
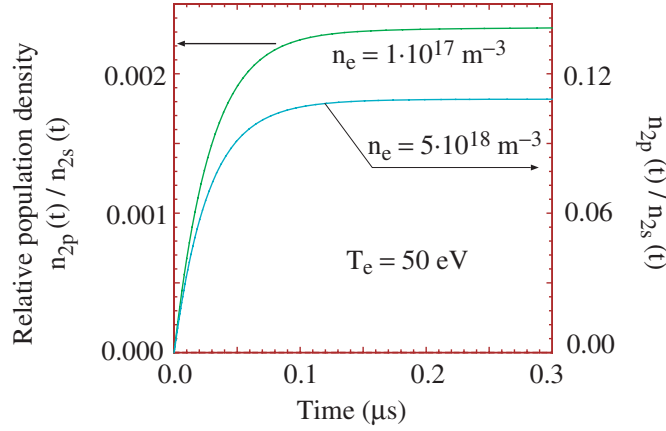
Figure 3. Temporal development of the relative population density, $n_{2p}(t)/n_{2s}(t)$, calculated using a collisional radiative model for two different electron densities: $n_e = 10^{17}\,m^{-3}$ and $n_e = 5 \times 10^{18}\,m^{-3}$.

The rate coefficients used in this work are taken from [20, 21]. The energy levels, E_i, and the transition probabilities, A_{ij}, are taken from [24] and are known with high accuracy (<10%).

This rate system of equations was solved by a fifth-order *Runge–Kutta* method. The relative population density, $n_i(t)/n_1(t)$, of the 2p-state is shown in figure 3 for two electron densities, $n_e = 10^{17}\,m^{-3}$ and $n_e = 5 \times 10^{18}\,m^{-3}$, as a function of time. The electron temperature is set in both cases to 50 eV. After a relaxation time of approximately $t_{rel} = 0.2\,\mu s$ the population density of the 2p-state reaches a stationary phase. This is the theoretical limit for the time resolution of the detection system. Based on the Nyquist criterion, an upper frequency limit of 2.5 MHz follows. It appears to be sufficient according to the experimental results, which show that only frequencies up to ∼100 kHz must be resolved. With a relaxation time of $0.2\,\mu s$, the displacement of the excited atoms amounts to ≈0.3 mm for thermal lithium. That is more than one order of magnitude lower than the radial correlation length observed (see section 6.7). Only two states, the ground state and the 2p-state, may be considered for determination of the electron density. The question arises as to how large the influence of the states above the 2p-state is. The relative population densities, $n_i(t)$, under consideration of two states or nine states in a homogeneous plasma (collisional–radiative model) with $T_e = 50\,eV$ in the electron density range between $n_e = 10^{17}\,m^{-3}$ and $n_e = 10^{20}\,m^{-3}$ were computed and compared. Figure 4 shows the ratio of the population density in the 2p-state, calculated with the different models in the stationary phase. The deviation between the two models lies below 10% for electron densities below $n_e = 10^{19}\,m^{-3}$. At larger electron densities, the model with two states overestimates the population densities. This is due to the fact that the losses by ionization processes from the excited states begin to play an essential role. The measuring method is thus applicable up to an electron density of $n_e = 5 \times 10^{18}\,m^{-3}$.

4. Experimental arrangement

In the SOL of TEXTOR, the density fluctuations have been recorded with high spatial and temporal resolution using a double Li-beam based on the method described earlier. The main parts of this diagnostic are the neutral Li-particle source and the detection system (observation optics, optical fibres, interference filters, detectors, control and data acquisition system).
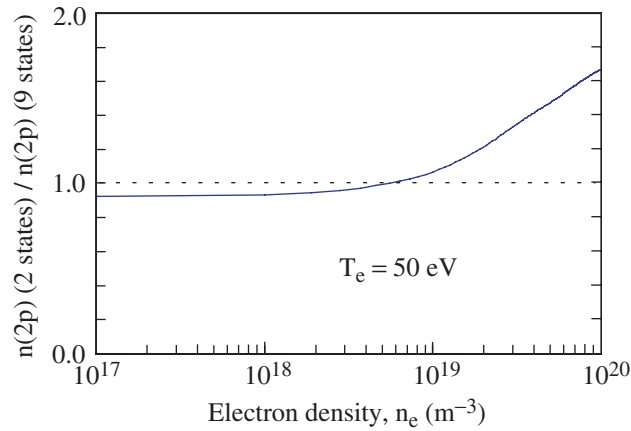
Figure 4. Comparison of calculations with the collisional–radiative model for two levels and nine levels.

4.1. The neutral thermal Li-beam

The fluctuations have a strong spatial anisotropy: in particular different parallel and perpendicular properties with respect to the direction of the magnetic field are pronounced. It was found in ASDEX from measurements made with two Langmuir probes [25, 26] that the fluctuations of the ion saturation current are in phase along a magnetic field line over a distance of more than 10 m, whereas the correlation length perpendicular to $\vec{B}$ is on the order of millimetres. Based on these observations, an experimental set-up is needed which allows us to determine the radial and poloidal correlations of fluctuations with a resolution of 1 mm, simultaneously. For this purpose, a source with two Li-atomic beams was developed at TEXTOR, allowing three-dimensional analysis of the spatial structures in the SOL.

4.1.1. Source of thermal Li-atoms.   The thermal lithium beams were produced using an oven in TEXTOR. The oven is made of a stainless steel housing heated resistively by a thermocoax and the temperature is controlled by a Ni–CrNi-thermocouple. The oven is filled with a solid Cu/Li alloy and the typical operating temperature is approximately 700°C. The alloy contains about 2.5% (weight) of Li. The copper remains in the solid state for temperatures below 1000°C, whereas the lithium component is sublimated. The oven has two extraction holes of 5 mm diameter. The flux density of the evaporated neutral lithium depends on the process of diffusion from the bulk to the surface, which can be controlled by the temperature of the alloy. The oven design is shown in figure 5.

The advantage of these sources compared with liquid Li-sources is the production of a continuous flux for a long time and the easy handling of solid material. The large Li-inventory in the oven head allows an operation of about 100 h without exchange of the alloy. After the lithium is exhausted, the alloy can be exchanged easily for a new one. Moreover, the Li-atoms can be injected in any direction, since the oven can be mounted in any position.

4.1.2. Li-flux measurements.   Figure 6 shows the flux densities of evaporated neutral lithium in an Arrhenius plot. This measurement was performed with a quartz microbalance [27]. The quartz plate (of circular shape and 6 mm in diameter) was mounted at a distance of 100 mm from the oven and the absolute lithium flux density was calculated from the decrease in
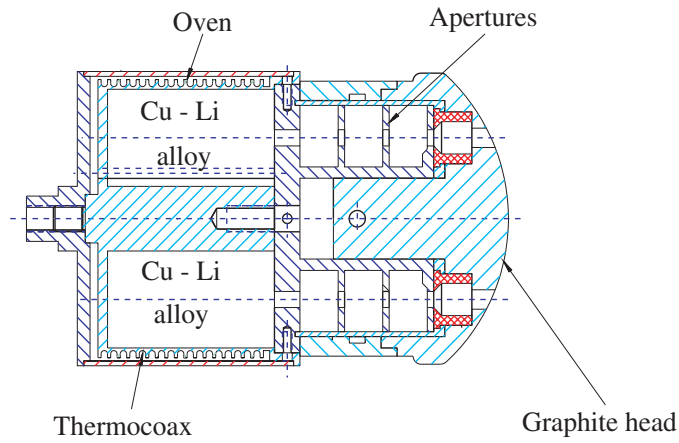
**Figure 5.** Design of the thermal double Li-beam oven.
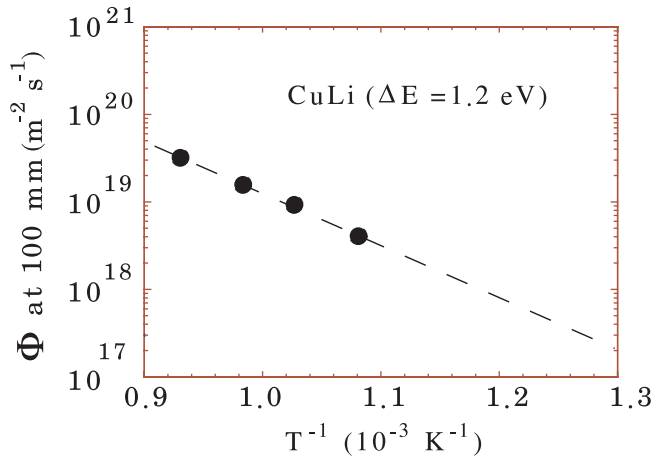
Figure 6. The Li-flux densities measured at a distance of 100 mm between the oven and the measuring point. The Li-fluxes have been measured using a quartz microbalance.

frequency of the quartz oscillator. The oven temperature was monitored using a thermocouple and kept at a constant level by a feedback system. Li-flux densities of $5 \times 10^{18}\,\mathrm{m^{-2}\,s^{-1}}$ have been achieved at a temperature of 700°C. The mean velocity of the lithium atoms is $\approx 1.7 \times 10^3\,\mathrm{m\,s^{-1}}$. From this, one gets a density of Li-atoms of $\approx 3 \times 10^{15}\,\mathrm{m^{-3}}$. It is at least a factor 100 lower than the electron density in the SOL and, consequently, the influence of the Li-beam on the plasma is negligible. The Li-flux can be kept at this constant level for more than 100 h.

4.1.3. Divergence of the beams. The resolution of the fluctuation wavelength, Λ, is limited by the width of the beams. The effect of the finite width of the beams is described in section 6.4.

The design of the Li-oven includes apertures for determining the beam divergence. The width of the beams was measured in the laboratory by laser-induced fluorescence [28]. Figure 7 shows the results. A single beam has a width of 10 mm at a distance of 100 mm from the oven. Since the oven is located inside the graphite head, the source can be moved in, close
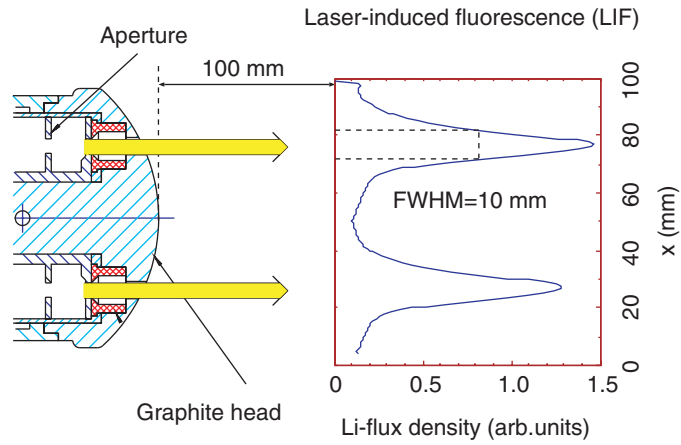
Figure 7. Li-flux density profile at a distance of 100 mm between the Li-source and the observation point.
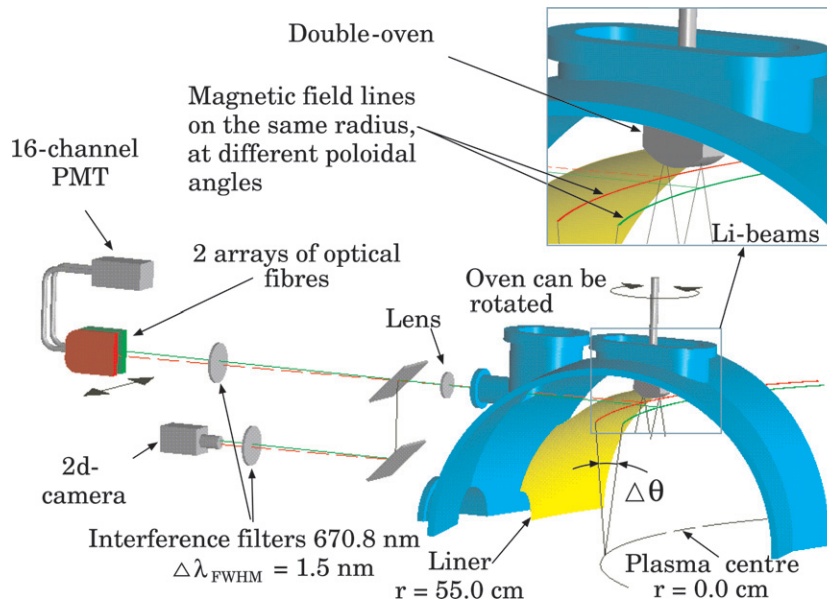
Figure 8. Observation system of the Li-beam diagnostic at TEXTOR-94.

to the plasma. The observation volume should obviously be as close as possible to the oven in order to reduce the width of the Li-beams, i.e. to get a better resolution of the fluctuation wavelength. An increase in the beam divergence to non-tolerable values is caused by coverage of the graphite head by lithium, which occurs after about 100 h of operation. It is then necessary to clean the head.

4.2. Observation system

The experimental set-up of the injection and observation system is shown in figure 8. Parallel to the rotation axis of the oven, two Li-beams are vertically injected down into the plasma from

the top of the vessel. The projection lengths of the distance between the beams (50 mm) in the toroidal and poloidal directions are varied by rotation of the oven in steps of $\Delta\alpha = 3.75°$. This arrangement allows a measurement on the very same magnetic flux surfaces at different poloidal angles (figure 8). The separation length of the beams is much shorter than the toroidal correlation length and the effects along a magnetic field line can be neglected. The line radiation along the beams is imaged onto two linear arrays of optical fibres which can be adjusted according to the toroidal projection of the beam positions. A range of 17 mm in the plasma boundary is covered by eight equidistant fibres. The two arrays are shifted vertically between several identical discharges to obtain the whole radial emission profiles of the beams. The line radiation at 670.8 nm is selected by a three-cavity interference filter with a bandwidth of 1.5 nm in front of the arrays. Every fibre leads to an individual multiplier (Hamamatsu R928) which is screened by μ-metal to reduce the influence of the magnetic stray field. Additionally, all the detectors are mounted in a box with soft iron walls of 2 mm thickness. The anode of each multiplier is connected to an impedance transducer of 50 Ω (line driver) to reduce the noise of the signal by the electrical pick-up on the cable. The electrical signals are digitized with a synchronized sampling rate of 500 kHz in analogue-to-digital converters (ADCs) with a resolution of 12 bits and stored into memories over a period of 2 s.

Every multiplier has a different sensitivity, and the linear dependence of the sensitivity between the photon flux and the voltage at the ADCs was recorded experimentally. The spatial channels were relatively calibrated with the signal from the additional 2d-camera (see picture). For the purpose of this comparison, the multiplier signals are integrated over 20 ms and normalized to the corresponding spatial channel on the camera frames.

The radial distribution of the Li-emission line and the deduced n_e profiles are measured with a 2d-camera of 128×128 elements every 20 ms simultaneously. For this measurement, 10% of the total emission radiation was extracted with a beam splitter and directed into the camera. The combination of measurements with the photomultiplier and 2d-camera allows determination of the absolute fluctuations, $\tilde{n}_e$.

Sixteen channels are required for detection of the fluctuation signals. The absolute calibration of every individual channel is always complicated and causes a measurement error during evaluation. The splitting of the emission signal onto two detection systems has the advantage that the mean value of the photomultiplier signal can be calibrated to the mean value of the 2d-camera signal. As a result, the amplitudes of the density fluctuations could be determined absolutely.

Interference filters are used for selection of the Li_{2p-2s}-emission radiation. The filters are positioned directly in front of light guides arrays. Three-cavity interference filters with a central wavelength of 670.8 nm and a bandwidth of 1.5 nm are used. Due to the existence of two beams and two arrays, this arrangement has radial and poloidal resolution simultaneously.

5. Experimental identification of the magnetic field line through both Li-beams

The important parameter in the experiment with a rotating double beam is the *poloidal* angle, $\Delta\psi$, between two magnetic field lines, which penetrate the Li-beams at the same plasma radius (ψ is the angle of the field line with respect to the toroidal direction). The initial condition $\Delta\psi = 0$, where one field line passes both Li-beams, has to be identified experimentally. Then the angle $\Delta\psi$ can be easily calculated for any poloidal displacement of the beams.

The beams are observed between plasma radii of 440 and 500 mm. In this range, for $B_{t0} = 2.25$ T, $I_p = 350$ kA, $R_0 = 1.75$ m and $\theta = 90°$, the angle ψ varies between 3.6° and 4.0°. This slight variation can be neglected because the oven is turned around its axis in discrete
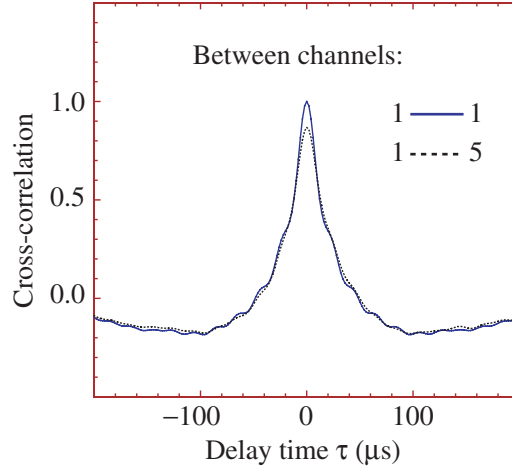
Figure 9. Auto- and cross-correlation functions between channels at the same plasma radii.

angles of $\Delta\alpha = 3.75°$. The location of the beams with respect to the magnetic field lines was determined at TEXTOR-94 experimentally, based on the facts that [25, 26]:

- the fluctuations along the magnetic field line are in phase and
- the correlation length along the magnetic field line is long (at ASDEX, a maximal correlation of more than 0.8 at a distance of about 10 m was recorded [26]).

The oven was turned and the cross-correlation between the two beams examined. Figure 9 shows the largest achieved cross-correlation between two experimental points, which are on the axes of two beams; it amounted to ≈ 0.95. In this case, the maximum value of 1 was not achieved because the oven could only be rotated with discrete steps and the magnetic field line did not totally penetrate both Li-beams in the same way. For this position of the oven, the same magnetic field line penetrates through both beams.

6. Experimental results and discussion

6.1. Determination of the electron density profiles

A contour plot of the 2d-camera signal is presented in figure 10(*a*). The x-axis and the y-axis correspond to the toroidal and radial coordinates, respectively. The total recording time was 2.0 s during the stationary phase with constant plasma parameters. For these measurements, the double oven was located at plasma radius $r = 530$ mm. In this case, the poloidal angle between the beams was $\Delta\psi = 3.75°$. This corresponds to a poloidal separation of ≈ 3.3 mm. At a plasma radius of ≈ 490 mm, the intensity shows a local maximum. At this location, the product $n_{\text{Li}}n_{\text{e}}$ is compensated and then dominated by ionization losses. The Li-atoms are completely ionized for $r < 440$ mm.

Such measurements were performed for every discharge for a continuous check of the Li-beam width. The Li-flux density at a plasma radius of $r = 480$ mm as a function of the toroidal coordinate is presented in figure 10(*b*). Here the FWHM of the beams is ≈ 11 mm. This corresponds to a measurable wavenumber $k_\theta < 0.6$ mm^{-1}.

The radial distribution of the emission line is presented in figure 11. The electron density profile was calculated from the emission line as shown in the section 2.3. At the LCFS
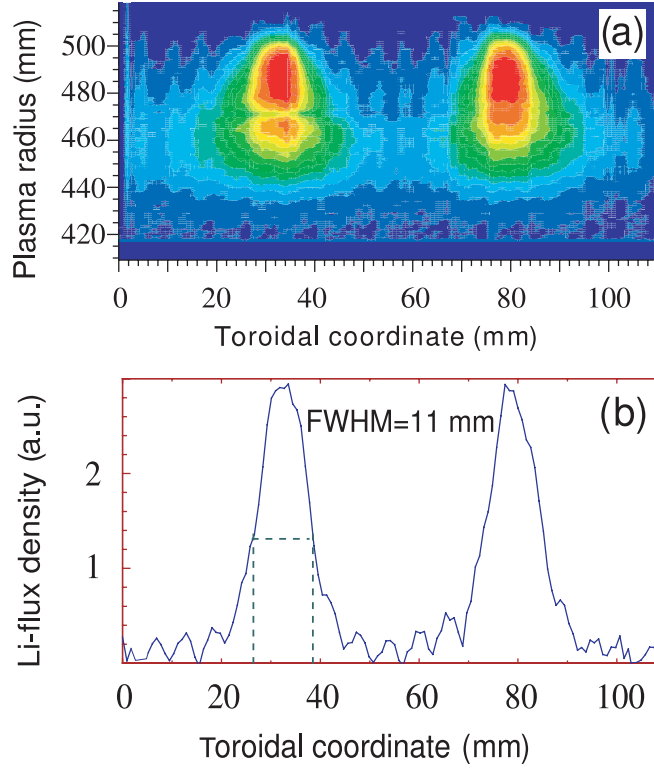
Figure 10. (*a*) Radial and toroidal distributions of the Li_{2p-2s}-emission line which was measured using the 2d-camera; the double oven was located at a plasma radius of $r = 530$ mm, $\Delta\psi = 3.75°$. (*b*) The Li-flux density as a function of the toroidal coordinate at a plasma radius $r = 480$ mm.

($r = 460$ mm) the electron density is about an order of magnitude below the electron density in the plasma centre.

6.2. Absolute values of density fluctuations in space and time

The electron density was measured with spatial and temporal resolution. The signals, $f(r_i, t_j)$, are the digitized voltage of the photomultipliers, and r_i describes the position of the observation volume. By measurements of the electron density at several radially separated channels, a complete spatio-temporal measurement can be obtained.
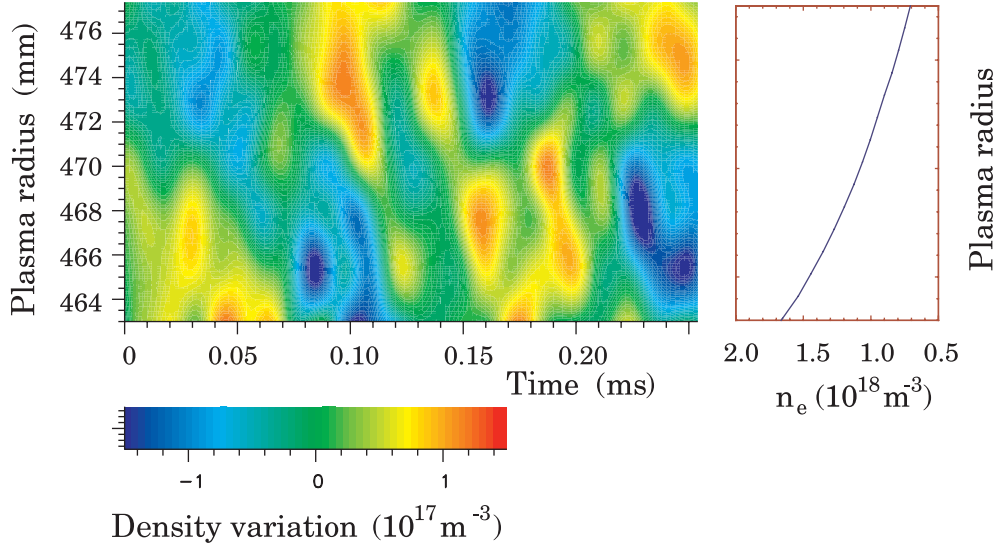
Figure 12 shows the absolute deviation of the electron density from the mean value $n'_e(r, t) = n_e(r, t) - \bar{n}_e(r)$ over a time period of 0.25 ms, as a function of time. The measurements were carried out with a time resolution of $2\,\mu s$ and a spatial resolution of ≈ 2 mm. The contour plot of density fluctuations is coded by a colour scale. The line-averaged electron density was $\bar{n}_e = 2 \times 10^{19}\,m^{-3}$. The local electron density profile, $\bar{n}_e(r)$, which was determined by the 2d-camera, is shown on the right-hand side of figure 12.

We can see that some structures reappear in the adjacent channels. However, they are displaced proportional to the channel spacing within a given time. These are structures which move into the radial direction during their lifetime and they can be observed in several channels. There are also events whose radial expansion is smaller than the channel separation.

The structures propagate, in the case shown, with a velocity of some $100\,m\,s^{-1}$ inwards.
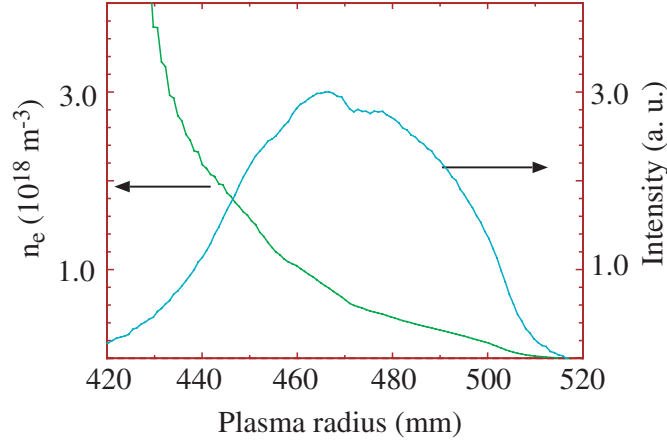
Figure 11. The radial distribution of the Li$_{2p-2s}$-emission line and the electron density profile in the SOL at TEXTOR-94 (typical case for an ohmic discharge with $\bar{n}_e = 1.5 \times 10^{19}$ m^{-3}, $I_p = 350$ kA, $B_t = 2.25$ T).


Figure 12. The absolute deviation of the electron density from its mean value.

6.3. Spectra of fluctuations

The cross-power and phase spectra as well as the coherence offer a further step for understanding the fluctuations. They are calculated by a Fourier transformation [29]. Figure 13 shows the auto-power spectrum (*a*) of one channel and the cross-power spectrum (*b*) between this and one radially adjacent channel. The radial distance between the two locations of the observed signals was 2.4 mm. The signals were sampled with a frequency of $\nu_A = 500$ kHz in a finite time period (≈ 1.05 s) during the stationary phase of an ohmic discharge.

The spectra are not presented up to the Nyquist frequency, ν_{Nyq}; they show only the range of interest for the fluctuations up to 100 kHz. The higher frequency range shows no changes
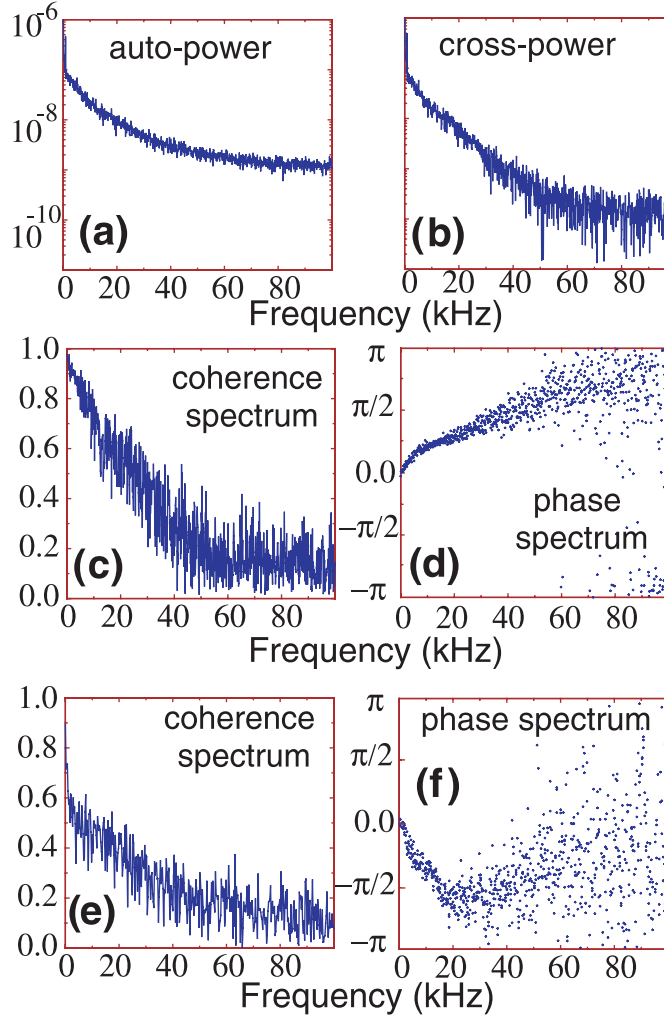
Figure 13. Auto-power spectrum (*a*) of the measurement signal of one channel and the cross-power spectrum (*b*) between this and a radially adjacent channel; coherence (*c*) and phase spectrum (*d*) of measurement signals, which are radially separated by a distance of 2.4 mm. Coherence (*e*) and phase spectrum (*f*) of measurement signals, which are poloidally separated by a distance of ≈10 mm.

any more: the spectra above 100 kHz only contain uncorrelated noise. This follows from the auto-correlation function of the measured signal components above 100 kHz, where a $\delta(\tau)$ function is received.

The spectral power of the observed fluctuations decreases monotonously for higher frequencies. Because of the small channel spacing of $\Delta r = 2.4$ mm, the spectra shown in figures 13(*a*) and (*b*) are hardly different at small frequencies. We can see the clear deviation of these spectra in the range of the higher frequencies, where the power of perhaps still available coherent signal fractions is below the detection limit. The cross-power spectrum shows lower values at higher frequencies because the two independent sources of noise have no correlation.

Additionally figure 13 shows the coherence (*c*) and (*e*) and phase spectra (*d*) and (*f*) of two channels which are spatially separated. The coherence decreases monotonously for higher frequencies. Above about 50 kHz a mean value of ≈0.1 is achieved, which corresponds to

the expected level for a random signal in the case of the selected time window and average factor. Therefore, we can speak of coherent fractions up to a frequency of ≈ 50 kHz. The phase spectrum, calculated from two signals, is also presented in figure 13(d). The radial separation, Δl_r, of these signals was 2.4 mm, and the poloidal separation Δl_θ was 0. The phase spectrum is only valid as far as the coherence is clearly above the statistical level, which means up to a frequency of ≈ 50 kHz; above that, the phase values have a random distribution between $-\pi$ and π.

Due to the poloidal separation of the two beams, the coherence and phase spectra could be simultaneously investigated from the two signals, which are poloidally separated by 10 mm. The spectra are presented in figures 13(e) and (f). The amplitude of the coherence spectrum in the case of the poloidal arrangement of the light guides is considerably lower than in the radial arrangement, which can be explained by the decrease in the distance Δl_θ. The phase spectrum is valid up to a frequency of ≈ 20 kHz.

The group velocity is quantitatively evaluable only for those frequency ranges in which the phase spectrum can be approximated by a straight line. This is possible for radially separated channels, in two ranges, from 0 Hz to ≈ 10 kHz and from ≈ 10 to 50 kHz, and for poloidal separation up to 20 kHz. In these ranges, the group velocities can be determined: $v_g^r \approx 1.5 \times 10^2$ m s^{-1} and $v_g^r \approx 5.0 \times 10^2$ m s^{-1}, respectively, and $v_g^\theta \approx 1.2 \times 10^3$ m s^{-1}.

Considering the arrangement of the light guides and of the orientation of the magnetic field towards the measurement point, the fluctuations propagate with a poloidal velocity in the direction of the diamagnetic drift of the ions and with a radial velocity inwards. In the SOL of TEXTOR-94, the diamagnetic drift velocity of the electrons can be estimated with good approximation:

$$v_{De} = \frac{k_B T_e}{eB} \left(\frac{1}{\lambda_n} + \frac{1}{\lambda_T} \right), \tag{15}$$

where λ_n and λ_T are the e-folding lengths for density and temperature. With $\lambda_n \approx \lambda_T \approx 30$ mm, $T_e = 50$ eV and B ($r = 460$ mm) $= 2.25$ T, the drift velocity of the electrons is $v_{De} \approx 1.4 \times 10^3$ m s^{-1} for a plasma radius $r = 460$ mm. It is of the same order as the determined poloidal group velocity, v_g^θ.

6.4. Influence of the beam width on the spectra

In order to understand the influence of the beam width on the resolution in $\vec{k}$-space, one considers a simple model as presented in figure 14. The beam is injected in the radial direction and observed in the poloidal direction. Every channel collects the light from an observation volume with a radial and toroidal extension, $\Delta_r = 1$ mm and $\Delta_\varphi = 10$ mm, which is defined by the observation system. The poloidal extension, Δ_θ, is determined by the width of the beam.

Only fluctuations whose wavelengths are larger than the projection of the observation volumes on the $\vec{k}$-vector can be measured. Shown is the critical case in which the wavelength and projection length are identical. The toroidal component of the $\vec{k}$-vector can be neglected (see section 5), and the $\vec{k}$-vector contains the radial and poloidal components. The maximum measurable wavenumbers can be derived: $k_r^{max} \approx 6.2$ mm^{-1}; $k_\theta^{max} \approx 0.62$ mm^{-1}. It was assumed here that $2\pi / k_r^{max} = \Delta_r$ and $2\pi / k_\theta^{max} = \Delta_\varphi$. One sees that the resolution is limited by the beam width in the poloidal direction.

The influence of the beam width on the auto-power spectrum was investigated experimentally. Figure 15 shows spectra for two cases with beam widths of 20 and 50 mm. The width of the beam was adjusted by changing the distance between the Li-source and the observation volume. The measurements were carried out in two ohmic discharges under the
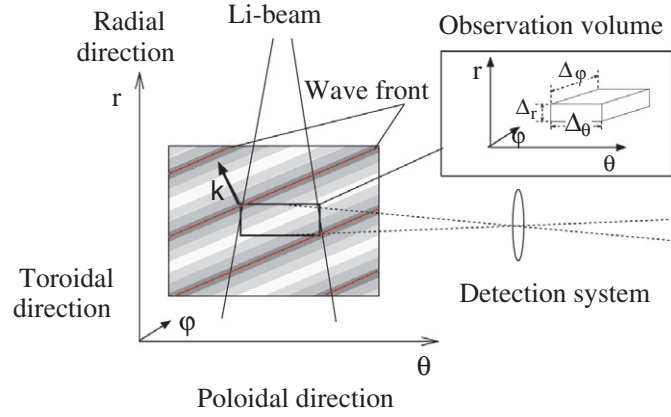
Figure 14. The influence of the beam width on the resolution in $\vec{k}$-space.
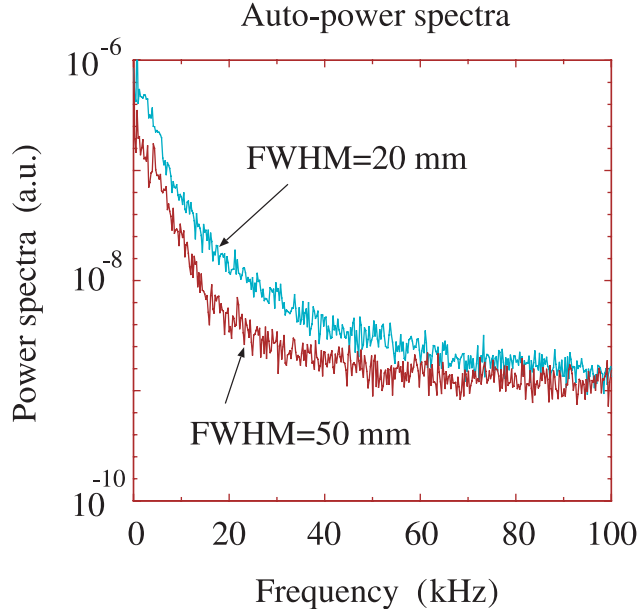

**Figure 15.** Auto-power spectra of signals with different beam widths.

same conditions as described earlier. For comparison, the spectra were normalized by the mean square value of the signals. In this case, the integral over frequency (from $-\nu_{\mathrm{Nyq}}$ to ν_{Nyq}) is the square of the relative standard deviation of the electron densities $(\tilde{n}_{\mathrm{e}}/n_{\mathrm{e}})^2$. One can see that the fluctuation amplitudes decrease with increasing width. The high frequency range is especially affected as far as it is above the noise level.

6.5. Radial variation of the relative and absolute fluctuation amplitudes

The absolute and relative fluctuation amplitudes were measured simultaneously using the techniques described in section 4. Using the 2d-camera, the mean value of the electron density
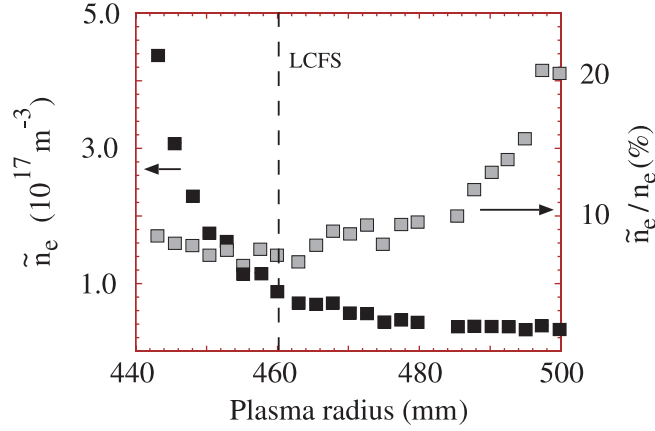
Figure 16. Radial variation of the relative and absolute fluctuation amplitudes of electron density.
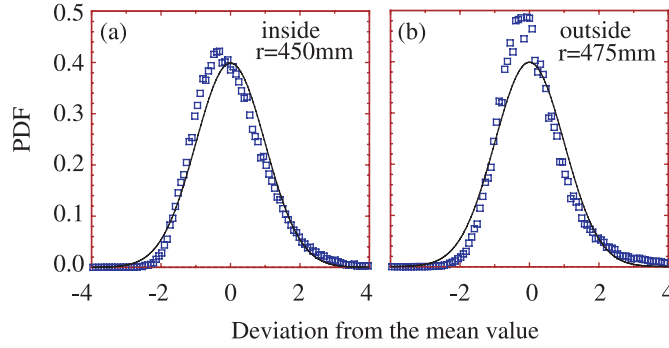
Figure 17. Comparison of the probability density function (PDF) of a measurement of the electron density ($\square$) with a Gaussian distribution (——) at two measurement points: within (a) and outside (b) the LCFS.

profile and, simultaneously at eight radial positions for every Li-beam, two profiles of the relative fluctuation amplitudes can be determined.

Figure 11 shows the radial distribution of the Li_{2s-2p}-emission and the corresponding electron density profile. The radial variation of the relative fluctuation amplitudes is presented in the figure 16. The measurements were made in a series of three ohmic discharges with the same plasma parameters described above. The relative error due to photon statistics was $\approx 2\%$.

Here one sees a continuous increase in the relative amplitudes, $\tilde{n}_e/n_e$, to higher plasma radii: from $\approx 8\%$ at the LCFS ($r = 460$ mm) up to $\approx 20\%$ at $r = 500$ mm. The absolute amplitude of the fluctuations should be calculated from the mean value of the electron density and the relative fluctuation amplitudes (see figure 16). They increase with smaller radii.

6.6. Distribution function of fluctuations

The calculation of the *probability density function* (PDF) is a further step towards understanding the fluctuations. Figure 17 shows the PDFs for the electron densities which were measured at two places: inside and outside the LCFS at radii $r = 450$ and 475 mm. The PDF is plotted as a function of the fluctuation amplitude normalized to the standard deviation, σ, of the PDF.
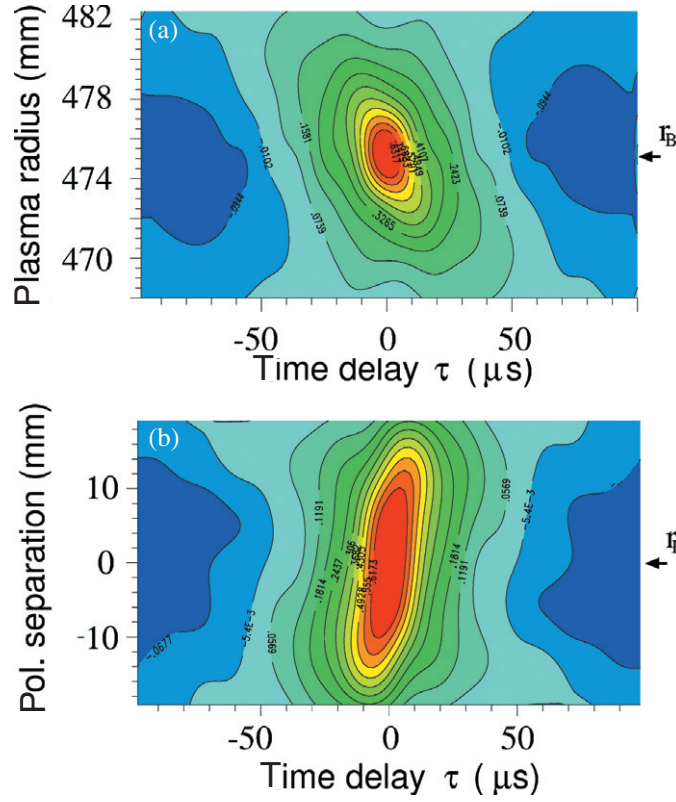
Figure 18. Radial (*a*) and poloidal (*b*) correlation functions of the electron density fluctuation outside the LCFS ($r = 475.0$ mm).

In addition, a Gaussian distribution $P(v) = 1/\sqrt{2\pi} \exp\left(-v^2/2\right)$ is presented. The shapes of the PDFs shown refer to a deviation from the Gaussian distribution function. The positive deviations of the signal amplitude from the mean value deviated more strongly than the negative deviations. The *skewness* ($\int_{-\infty}^{\infty} (x - x_0)^3 p(x) \mathrm{d}x / \sigma^3$, where x_0 is the mean value of x and p is the PDF) and *kurtosis* ($\int_{-\infty}^{\infty} (x - x_0)^4 p(x) \mathrm{d}x / \sigma^4$) are 0.57 and 3.44 within the LCFS and 0.98 and 5 outside.

6.7. Radial and poloidal structure of the electron density fluctuations

The radial cross-correlation function between the signals $f(r_i, t)$ and $f(r_B, t)$ with a fixed r_B (reference signal) delivers the spatial–temporal correlation function.

The radial correlation function of the electron density fluctuations is presented in figure 18(*a*). With a distance of 2.4 mm between channels, the seven active channels covered 14.4 mm. The plasma radius of the reference signal, r_B, was 475.0 mm. The levels of the correlation function are drawn by equidistant lines. The degree of correlation is coded in a colour scale (red maximal, blue minimal).

This figure shows a 'correlation structure' which is extended along a straight line. As shown in appendix A, the inclination of this structure gives the velocity of the fluctuations in the radial direction, in this case $v_r \approx 1.4 \times 10^2$ m s^{-1}. The slope indicates an inward velocity of the fluctuations. However, as shown in appendix A, if the turbulent structures are inclined in the poloidal–radial plane, their movement in the poloidal direction could strongly influence
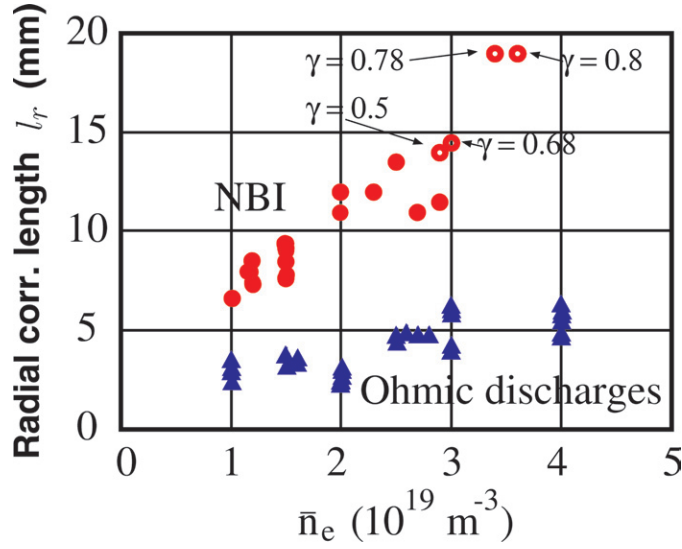
Figure 19. Radial correlation lengths as functions of $\bar{n}_e$ at a plasma radius $r = 466$ mm: the triangles represent discharges with ohmic heating, dots discharges with additional neutral beam heating and circles discharges with neutral beam heating and neon injection, where $\gamma = P_{rad}/P_{heat}$ is the ratio between the total radiated power and total heating power.

the absolute value of the radial velocity. We will therefore call this radial velocity an apparent velocity.

This presentation also delivers information on the lifetime or correlation time, τ_L, and on the spatial extension or correlation length, L_r. These values of the correlations decrease after some millimetres; the radial correlation length is ≈ 3 mm. For time delays larger than 15–20 μs the correlation decreases very strongly. In appendix A it is shown how the lifetime of the fluctuation is determined. In this case it is ≈ 15 μs.

Because of the poloidal separation of the two beams, the poloidal and radial correlation functions can be determined. Figure 18(*b*) shows the cross-correlation for six poloidal separations, obtained in the same number of identical discharges. The poloidal angle between beams was changed from discharge to discharge. Two poloidally separated emission volumes were selected at a plasma radius $r = 475$ mm.

This presentation shows that the maximum of the correlation moves with an increase in the poloidal separation. This can be explained by a poloidal propagation velocity of the fluctuations. The inclination of the correlation shape gives a poloidal velocity of $\approx 1.0 \times 10^3$ m s^{-1}. The direction of motion can be determined from the sign of the time delay. The fluctuations propagate in the diamagnetic drift direction of the ions.

The radial and poloidal correlation functions shown in figure 18 construct a picture of short-living events. The lifetime or correlation time of these events is some 10 μs. The fluctuation propagates outside the LCFS with a poloidal velocity of $\approx 10^3$ m s^{-1} in the diamagnetic drift direction of the ions, and their apparent radial velocity is $\approx 1.4 \times 10^2$ m s^{-1} inwards. The poloidal correlation length is a factor 3–4 larger than the radial correlation length.

It cannot be decided whether the observed velocities were bulk velocities of the plasma or propagation velocities of the fluctuation, or any combination of the two. All diagnostics which measure the fluctuations are confronted with this problem.

Figure 19 shows the typical radial correlation length, l_r, found on TEXTOR-94. The correlation length is presented as a function of $\bar{n}_e$ for ohmic discharges and for discharges with
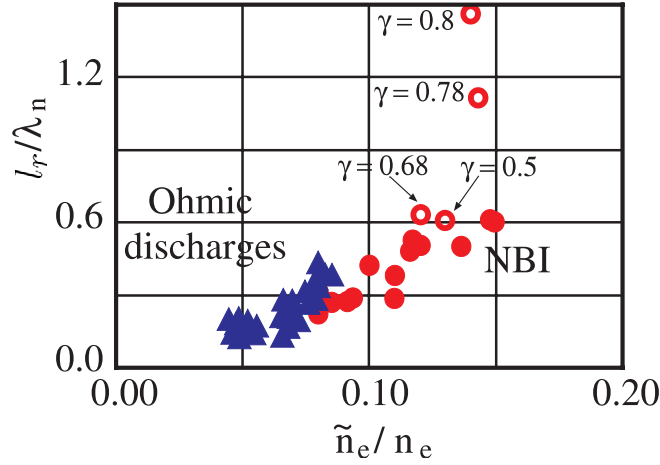
Figure 20. l_r/λ_n versus relative electron density fluctuation, $\tilde{n}_e/n_e$.

neutral beam injection (NBI) heating. These measurements were carried out at a plasma radius of $r = 466$ mm. We see that the correlation length with NBI-heating is larger than with ohmic heating alone in the range $\bar{n}_e = (1.0\text{--}4.0) \times 10^{19}$ m^{-3}. The increase in the radial correlation length with heating power has also been observed in the DIII-D tokamak [30]. Cooling by neon injection to achieve a large radiation level, γ, in discharges with NBI-heating leads to an additional increase in l_r.

Figure 20 shows the relation of l_r/λ_n as a function of the measured fluctuation level, where λ_n is the e-folding length of the electron density. The density fluctuations can be aproximated by $\tilde{n}_e/n_e \sim 0.25 \times l_r/\lambda_n$, which is consistent with the *mixing length estimation* within a factor of 4. This is valid for small fluctuation wavelengths $\lambda \ll \lambda_n$ and correspondingly for $l_r \ll \lambda_n$. For discharges with neon this estimation is not valid since $l_r/\lambda_n \geqslant 1$. The fluctuation levels in discharges with NBI are higher than in pure ohmic discharges.

In many papers [31–34], it has been shown that the theories of interchange turbulence in the SOL with dissipation by currents flowing through the potential sheath near the surface (*surface dissipation* (SD)) are usually capable of explaining the experimental data. Pressure perturbations cause perturbations in the current to the limiter which, in turn, vary the potential distribution and cause a fluctuation in the poloidal electric field. In this case, a positive pressure perturbation shifts towards domains with lower pressure, i.e. a convective instability exists.

The simplest theoretical models predict SD effects in the SOL to be dominant if the inequality $\alpha = (m_e/m_i)^{1/2}L/\lambda_e \ll 1$ is fulfilled, where m_e and m_i are the electron and ion masses, respectively, L is the connection length and λ_e is the electron mean free path. The left side of this inequality is approximately equal to the inverse ratio of the product of the longitudinal electric field, $E_\parallel$, and L to the Langmuir sheath potential $\approx T_e/e$ for floating conditions, i.e. it is the ratio of SD to volume dissipation (VD) by Coulomb collisions. The inequality usually holds for tokamaks with small and middle sizes. However, for a cold, dense edge plasma, this inequality is not valid.

In TEXTOR-94, with a connection length $L = 2\pi qR \approx 35$ m, the parameter α is in the range 0–0.4 for the plasma conditions described earlier. For discharges with neon, this parameter is about 1–2. This means that VD is comparable with SD. The radial correlation length is increased drastically with cooling by neon injection, and the level of the density fluctuations and λ_n increase slowly.

The excitation of current-convective (rippling) turbulence in the presence of impurities in addition to SD is more likely to happen in this case. The reason for the turbulence is that the density fluctuations of low-Z impurities in a dirty plasma result in Z_{eff} fluctuations, which in turn drive rippling instabilities. This possibility was discussed in [35, 36]. Note that under these conditions the radial correlation length is comparable with the e-folding length of the density. Such large dimensions of the convection cells do agree with the theoretical estimation in the frame of impurity-driven rippling turbulence. A further discussion of the experiments with cooling by neon injection can be found in [37].

6.8. Wavenumber spectra

The spectra can be determined as a function of wavenumber in the experimental arrangement as described in section 4. The measurements which supply the radial and poloidal wavenumber spectra are especially important. To make such measurements, the fluctuations must be observed at several radial and poloidal positions. This condition is fulfilled by two Li-beams which can be poloidally moved apart.

The use of the Fourier transformation is connected with some difficulties. From the eight equidistantly measured local points (distributed over the radial range), the calculated radial wavenumber spectrum will contain only four values with a resolution of $\Delta k_r \approx 0.37\,\text{mm}^{-1}$, which is insufficient for detecting the position of a maximum in the spectral power at low wavenumbers. To reach a reasonable k_r-resolution of about $0.02\,\text{mm}^{-1}$ an array of 120 equidistant measurement points is required, which could cover a range of 300 mm. In addition, homogeneity over the measured range is needed to perform the Fourier transformation, a requirement not fulfilled in the present case: the temperature and the density change strongly over a few centimetres. An evaluation of k-spectra by using the Fourier transformation is possible only with an arrangement of measurement points distributed in the poloidal direction (at the same radius). Such a poloidal wavenumber spectrum is demonstrated in [42], measured using a Langmuir probe with 20 poloidal distributed probe tips (47.5 mm covered). But, as mentioned in [42], this arrangement yields a resolution of $0.13\,\text{mm}^{-1}$ and is not sufficient for resolving a possible maximum at low wavenumbers.

A *two-point method* [38] was used for calculation of the wavenumber spectra. For this purpose, the signals of electron density fluctuations at three spatial positions $f(r_0, \theta_0)$, $f(r_0 + \Delta r, \theta_0)$ and $f(r_0, \theta_0 + \Delta\theta)$ were investigated. Using the two signals, which are displaced only radially, a radial wavenumber spectrum $S(k_r)$ could be obtained. The poloidal wavenumber spectrum $S(k_\theta)$ can be determined from the measurements with signals separated only poloidally. The measurements were performed within 2 s during the stationary phase of the discharge and divided into $M = 62$ shorter time intervals with a length of 32 ms. Using the wavenumber spectrum of each window, a spectrum as a function of frequency and wavenumber was reconstructed.

We must mention here two papers of Carlson [39, 40] though, where the *two-point method* was proven numerically. It was found that this method is convenient for obtaining the mean value of the wavenumber and the width of the spectrum but does not always give the real shape of the spectrum. We must therefore be very careful in discussions of the profile shapes. Thus we will discuss in this paragraph only the mean value of the wavenumbers and spectral widths.

Figure 21 shows in a double logarithmic scale the radial (bottom) and poloidal (top) wavenumber spectra. The three measurement points were located outside the LCFS at a plasma radius of $r = 472$ mm. The poloidal spectrum was calculated for five measurements with different poloidal positions and presented in the same figure. We can see that there is no clear deviation between these evaluations. Both spectra are normalized to the total power. Because

Poloidal and radial wavenumber spectra
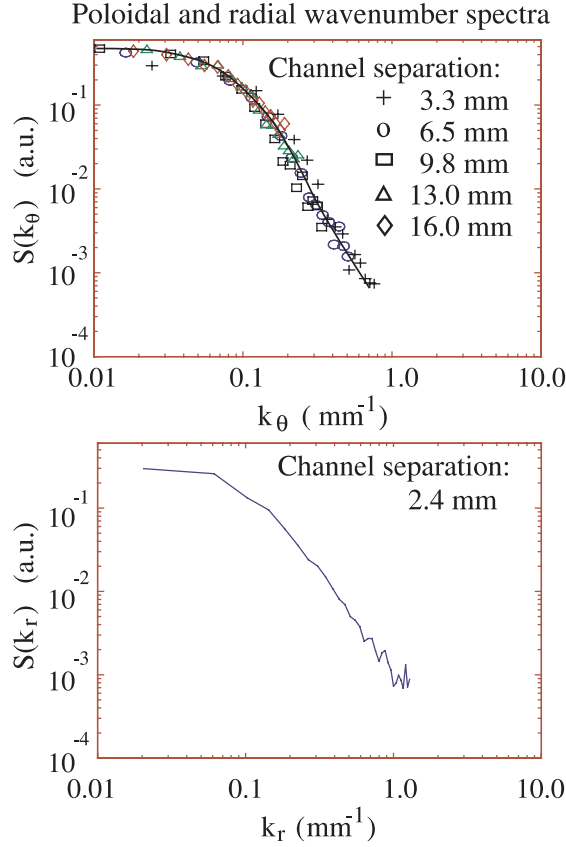
Figure 21. Radial (lower curve) and poloidal (upper curve) wavenumber spectra outside the LCFS.

the *two-point method* requires the independence of the two spectra, the power spectra can be calculated as a product of the radial and poloidal wavenumber spectra, $S(k) = S(k_r) \cdot S(k_\theta)$, as shown in figure 22. The spectrum is drawn here in the form of equidistant level lines. The power is colour-coded as previously.

The estimated mean values of the wavenumbers are $\bar{k}_r = 0.04 \, \text{mm}^{-1}$ and $\bar{k}_\theta = 0.03 \, \text{mm}^{-1}$, which satisfies $\bar{k}\rho_s \approx 0.04$–$0.1$, where ρ_s is the ion Larmor radius. We see that the mean value of the wavenumber has a positive radial and negative poloidal component. Taking into account the arrangement of the light guides and the orientation of the magnetic field at the measurement point, we can conclude that the fluctuations propagate with a poloidal velocity in the ion drift direction and with an apparent radial velocity inwards. The very same behaviour was observed using the correlation analysis presented in section 6.7.

The spectral widths, σ_k, of the wavenumber spectra are about 0.12 and 0.08 mm^{-1} for the radial and poloidal wavenumbers. It was found that the spectral width, σ_k, decreases with increasing central average electron density. This behaviour of σ_k is consistent with correlation lengh comparison, since the correlation length is proportional to $1/\sigma_k$ (see, e.g. [41]).

6.9. Conclusion

For measurements of both the *radial* and *poloidal* fluctuation structures with sufficient spatial and temporal resolution, a new technique using spectroscopic observations of atomic
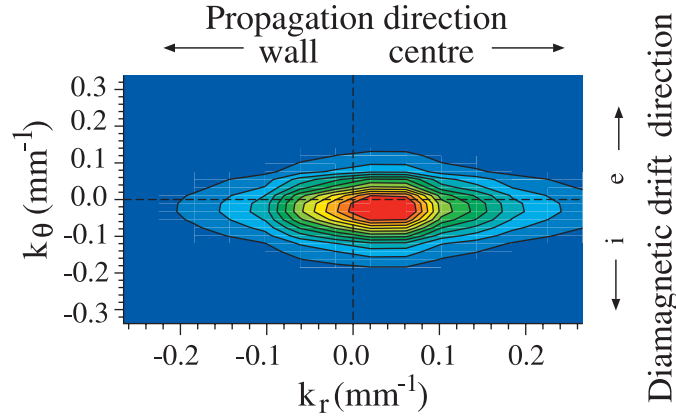
Figure 22. The radial and poloidal wavenumber spectra in the SOL of TEXTOR-94 (i = ion drift side, e = electron drift side).

beams for measurement of the electron density fluctuation in the SOL was developed, tested and applied on TEXTOR. *This new diagnostic allows studies of radial and poloidal fluctuation parameters, such as the correlation lengths, wavenumber and frequency spectra and propagation velocities and lifetimes.* The advantage of this method, as compared with traditional measurements with Langmuir probes, is that good spatial and temporal resolution can be achieved without disturbance of the plasma. Moreover, the application of continuous beams permits measurements over the whole discharge.

The determination of the radial and poloidal components of the fluctuation parameters was achieved by operation of two narrow Li-beams (FWHM ≈ 10 mm at a distance of 100 mm), which were separated by 50 mm. The beams of thermal lithium atoms were generated by a newly developed oven, which provides a long operation time and a high reliability. The atoms could be injected in any desired direction because the operation of the oven was insensitive to the positioning. The lithium atoms, with a mean velocity of about 1.7×10^3 m s^{-1}, were injected radially into the plasma edge, where they were excited and ionized by the plasma. The line radiation of the excited atoms was observed (resonance transition 2s–2p, $\lambda = 670.8$ nm), allowing determination of the electron density profiles and fluctuations. The measurements were performed with high temporal ($\Delta t \simeq 2 \, \mu$s) and spatial resolution ($\Delta_r \simeq 1$ mm in the radial direction and $\Delta_p \simeq 10$ mm in the poloidal direction).

A broad frequency band of $\nu \leqslant 100$ kHz and a wavenumber spectrum of $k_r, k_\theta \leqslant$ (0.5–1) mm^{-1} have been observed in the SOL of TEXTOR. Relative fluctuation amplitudes $\tilde{n}_e/n_e$ were found with levels of 5–10% inside the LCFS. Outside the LCFS within a radial range of 40 mm, they increased by a factor of 3–4.

Thanks to the poloidal separation of the two beams, the two-dimensional correlation functions and the corresponding radial and poloidal correlation lengths could be investigated. The radial correlation lengths in the SOL of TEXTOR varied between 3 and 6 mm in plasmas with ohmic heating and 7 and 13 mm with additional neutral beam heating. The measurements at all conditions indicate that the poloidal correlation length was a factor of 3–4 higher than the radial correlation length. The typical lifetimes of electron density fluctuations, as defined by a cross-correlation analysis, were 10–50 μs. Outside the LCFS, the fluctuations propagated poloidally in the direction of the ion diamagnetic drift with a velocity of $\approx 10^3$ m s^{-1}, and their apparent radial velocity was about $\approx 1.4 \times 10^2$ m s^{-1} inwards. Inside the LCFS, the fluctuations

moved in the other direction. The propagation direction of the fluctuations was reversed with reversed magnetic field.

Acknowledgments

Appendix A. Propagation velocity and lifetime of fluctuations

This section explains the determination of the propagation velocity (or the movement of the plasma) and the lifetime of the fluctuations from the spatial–temporal correlation function. Let us assume $f(x', t)$ is the measurement variable in the system of the plasma. If the plasma moves with a velocity υ in the x-direction, one measures the signal $f(x - \upsilon t, t)$. x and x' are the coordinates in the laboratory system and in the system of the plasma, respectively. The connection between x and x' is given by a Galilean transformation, i.e. $x = x' + \upsilon t$. The cross-correlation function between two channels a distance d apart in the laboratory system can be written as

$$P(d, \tau) = \int_{-\infty}^{\infty} f(x - \upsilon t, t) f(x - \upsilon t + (d - \upsilon \tau), t + \tau) \mathrm{d}t$$

$$= \int_{-\infty}^{\infty} f(x', t) f(x' + (d - \upsilon \tau), t + \tau) \mathrm{d}t = P'(d - \upsilon \tau, \tau), \quad \text{(A.1)}$$

where $P'(d - \upsilon \tau, \tau)$ is the cross-correlation function at a distance $d - \upsilon \tau$ in the plasma system. We can easily see from equation (A.1) that $P(0, 0) = P'(0, 0)$. One obtains the same relation between the normalized correlation functions in the laboratory and in the plasma system:

$$\mathrm{cor}(d, \tau) = \mathrm{cor}'(d - \upsilon \tau, \tau). \quad \text{(A.2)}$$

The cross-correlation function $\mathrm{cor}(d, \tau)|_{\tau = \mathrm{const}}$ shows a maximum at the location $d^{\max} = \upsilon \tau$. This follows from the characteristic of the correlation functions for all d.

$$\mathrm{cor}'(0, \tau) \geqslant \mathrm{cor}'(d - \upsilon \tau, \tau) \quad \text{(A.3)}$$
$$\parallel \qquad\qquad\qquad \parallel$$
$$\mathrm{cor}(\upsilon \tau, \tau) \geqslant \mathrm{cor}(d, \tau). \quad \text{(A.4)}$$

The velocity of propagation of the fluctuations can be determined from the relation $\upsilon = d^{\max}/\tau$.

Figure 23 shows the radial correlation function $\mathrm{cor}(d, \tau)$ that was determined with the radially separated channels. The function is drawn here in the form of equidistant contour lines. The correlation is coded by colour. The plasma radius of the reference signal was at $r_B = 475.5\,\mathrm{mm}$ ($d = r - r_B$). In order to determine the velocity of propagation, one selects a contour line (e.g. $\mathrm{cor}(d, \tau) = 1/e$) and marks the vertical tangent to this contour line, perpendicular to the τ-axis. The contact point of the tangent with the contour line yields a channel spacing d_0 and a delay time τ_0. The correlation function $\mathrm{cor}(d, \tau)|_{\tau = \tau_0}$ reaches a maximum at the position d_0, i.e. $d^{\max} = d_0$. As a result, one calculates the radial component of the propagation velocity of the fluctuations:

$$\upsilon_r = \frac{d_0}{\tau_0}. \quad \text{(A.5)}$$
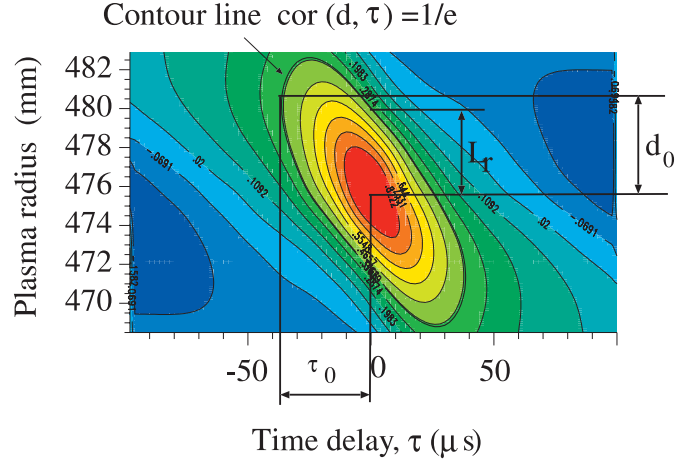
Figure 23. Determination of the lifetime τ_L ($=\tau_0$) of the correlation length in the radial direction, L_r, and of the radial component of the propagation velocity from the radial correlation function.
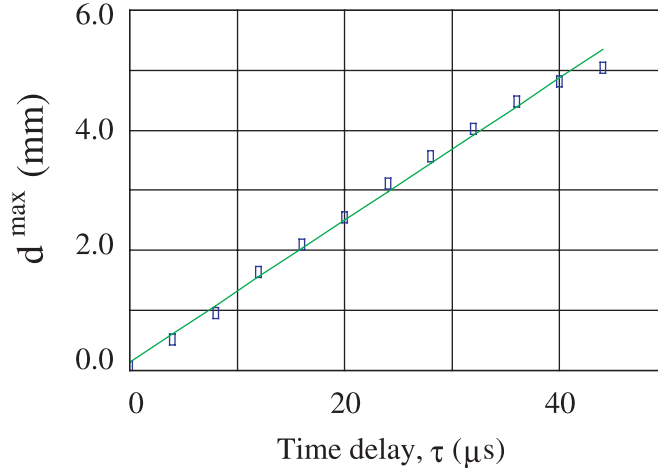

Figure 24. Determination of the radial component of the propagation velocity from radial correlation functions.

Due to the determination of $d^{\max}$ at different time delays $\tau_j[j = 1, \ldots, K]$, we obtain a function $d^{\max}(\tau_j)$ dependent on τ. Figure 24 shows values of $d^{\max}$ evaluated in such a way, as a function of the time delay, τ. It is a straight line with the angle $\upsilon = d^{\max}(\tau)/\tau$.

The determination of the velocity from the maximum of the cross-correlation functions in general leads to overestimated values because of the finite lifetime of the fluctuation events. For example, we consider a correlation function in the plasma system that consists of the product of two Gaussian functions:

$$\mathrm{cor}'(d, \tau) = \exp\left(-\frac{d^2}{L^2}\right) \cdot \exp\left(-\frac{\tau^2}{\tau_L^2}\right), \tag{A.6}$$
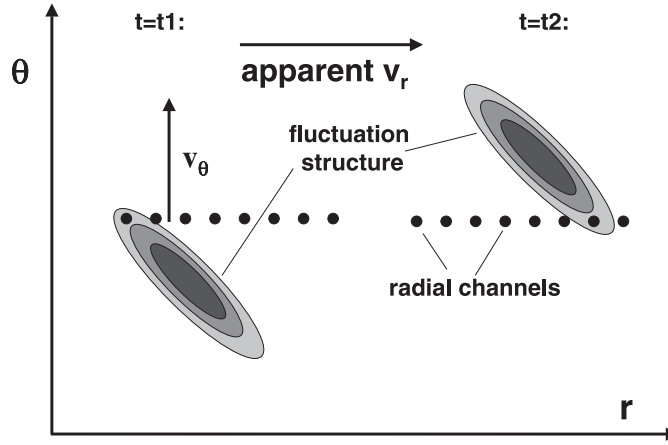
Figure 25. Inclined structures can give the impression of a radial movement when observed with a radial array of detectors, even if they move only in the poloidal direction.

where L and τ_L are the correlation length and lifetime of the fluctuations. The corresponding correlation function in the laboratory system is

$$\text{cor}(d, \tau) = \exp\left(\frac{-(d - \upsilon\tau)^2}{L^2}\right) \cdot \exp\left(-\frac{\tau^2}{\tau_L^2}\right). \tag{A.7}$$

The function $\text{cor}(d, \tau)|_{d=\text{const}}$ has a maximum at

$$\tau^{\max} = \frac{d\upsilon/L^2}{1/\tau_L^2 + \upsilon^2/L^2}. \tag{A.8}$$

The time delay $\tau^{\max}$ depends in general on the velocity of propagation, υ, on the correlation length, L, and on the lifetime, τ_L, of the fluctuations and takes values between 0 and d/υ. For $\tau_L \to \infty$, one gets the true velocity of propagation $d/\tau^{\max} = \upsilon$. If the fluctuations have a finite lifetime τ_L, one gets a value $d/\tau^{\max} > \upsilon$ which is too high: for instance for $\tau_L \to 0$, the velocity $\upsilon \to \infty$. The determination of the velocity from the maximum of the cross-correlation functions is not permissible because the lifetime of the fluctuations is some $10\,\mu\text{s}$.

The temporal width, τ_L, of the correlation function in the system of the plasma, $\text{cor}'(d, \tau)$, is defined in this work by

$$|\text{cor}'(0, \tau_L)| = \frac{1}{e}. \tag{A.9}$$

The width τ_L is defined as the lifetime. We can see from equation (A.2) that the auto-correlation function $\text{cor}'(0, \tau)$ in the plasma system is a cross-correlation function between two channels with distance $d = \upsilon\tau$ ($\text{cor}(\upsilon\tau, \tau) = \text{cor}'(0, \tau)$) in the laboratory system. The temporal width for the correlation maxima in the laboratory system becomes smaller for larger velocities.

If $\upsilon \to \infty$, the auto-correlation function switches into the auto-correlation function of white noise. The fluctuation events pass a fixed detector if the plasma moves, and the auto-correlation function $\text{cor}(0, \tau)$ gives us information on how long the events have been seen by the detector and not how long the fluctuations existed. It follows from this that the lifetime, τ_L, of the fluctuations cannot be determined using the auto-correlation function in the laboratory system. For determination of the lifetime of the fluctuations, one selects a contour line $\text{cor}(d, \tau) = 1/e$ (see figure 23) and marks the vertical tangent line. The tangent

touches the contour line at a location d_0 with a time delay τ_0. d_0 is, as shown above, identical to the value of $\upsilon\tau_0$. At the contact point

$$\text{cor}(d_0, \tau_0) = \text{cor}(\upsilon\tau_0, \tau_0) = \text{cor}'(0, \tau_0) = \frac{1}{e}. \tag{A.10}$$

It is easily seen from this equation that τ_0 represents the lifetime of the fluctuations, i.e. $\tau_L = \tau_0$.

If the turbulent structures are inclined in the poloidal–radial plane, the interpretation of velocity, however, demands special care. The inclination of the structures may originate from the radial shear of the poloidal velocity of the fluctuations in the plasma edge. The observed radial velocity can be the result of the projection of a poloidal velocity onto the radial axis. An example of such a projection is shown in figure 25. As the structure moves poloidally (upwards), the maximum that is detected by the set of radial channels moves radially, giving the impression of a radial movement. The measured radial velocity could thus be a mixture of radial and poloidal velocities. Measurements that have been performed with an angular array of Langmuir probes on W7-AS show that such effects can indeed dominate the radial velocity [42]: the measured radial velocity (apparent velocity) close to the LCFS was about $400 \, \text{m s}^{-1}$ and was aproximately equal to the poloidal velocity. As shown in this paper the real velocity was about $100 \, \text{m s}^{-1}$ and thus a factor of 4 smaller than the apparent radial velocity. For calculation of the real radial velocity, a two-dimensional correlation analysis is required. The deconvolution of the real velocity is discussed in detail in the following references [42,43] and is outside the scope of this paper.

The same argument is of course true for the reconstruction of the poloidal velocity. But because of the comparatively very low absolute value of the radial velocity the influence on the calculation of the poloidal velocity is negligible.

Appendix B. Deconvolution of instrumental profile

Two thermal Li-atomic beams are injected in the experiment radially into the plasma and observed perpendicular to the direction of propagation of the beam. The detectors register a radiation integrated along the beam cross-section so that the evaluated correlation function is influenced by the finite beam width.

If the true function and the atomic density distribution of a beam are given by the functions $f^w(x, t)$ and $A(x)$, the measured signal, $f^s(y, t)$, is determined by the integral

$$f^s(y, t) = \int_{-\infty}^{\infty} f^w(x, t) \cdot A(y - x) \mathrm{d}x. \tag{B.1}$$

The function $A(x)$ is the instrumental function. It describes the imaging from f^w into f^s. An apparent correlation function could be determined by measurement of the signals $f^s(y, t)$ and $f^s(y + d, t)$, which are separated poloidally around d.
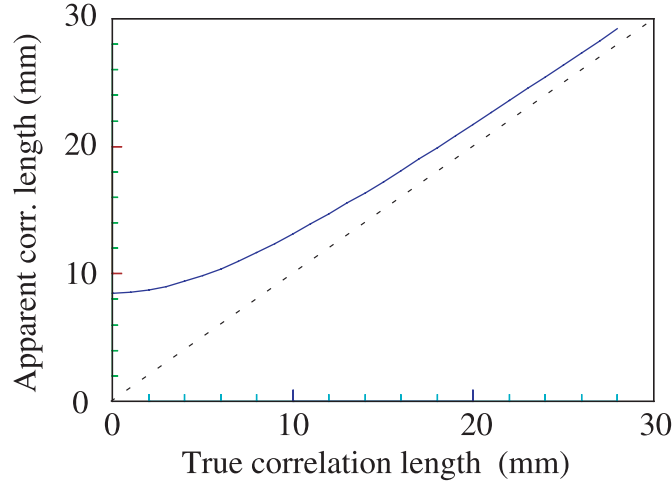
$$P^s(d, \tau) = \int_{-\infty}^{\infty} f^s(y, t) f^s(y + d, t + \tau) \mathrm{d}t. \tag{B.2}$$

The relation between the apparent and true correlation functions follows from equations (B.1) and (B.2).

$$P^s(d, \tau) = \int_{-\infty}^{\infty} A(y - x') \mathrm{d}x' \int_{-\infty}^{\infty} P^w(x' - x, \tau) A(y + d - x) \mathrm{d}x. \tag{B.3}$$

The normalized apparent correlation function, $\text{cor}^s(d, \tau)$, is

$$\text{cor}^s(d, \tau) = \frac{P^s(d, \tau)}{P^s(0, 0)}. \tag{B.4}$$

Figure 26. Apparent correlation length as a function of the true correlation length. It was assumed here that the true poloidal correlation function is described by a Gaussian distribution at a time delay $\tau = 0$.

Since the apparent correlation function, $\text{cor}^s(d, \tau)$, is observed, the true correlation function $\text{cor}^w(x, \tau)$ has to be determined. It is especially important to compute the true correlation length, L_θ^w. The poloidal correlation length evaluated using the apparent correlation function provides an overestimated value L_θ^s.

The apparatus function, $A(x)$, of the Li-beam diagnostic could be approximated very well by the function

$$A(x) = C \cdot \exp\left(\frac{-x^2}{s^2}\right) \qquad \text{with } s = 0.6, \qquad (B.5)$$

which corresponds to the FWHM of a beam of 10 mm. The factor $C = 1$ because a standardized correlation function is used.

In order to determine the true correlation length, we consider only the correlation functions, true and apparent, during a time delay $\tau = 0$. The latter is selected here in the form of a Gaussian function $\text{cor}^w(d, 0) = \exp(-(d/L_\theta^w)^2)$. The apparatus distribution is folded with the other function $\text{cor}^w(d, 0)$, both assumed as Gaussian functions; one gets a Gaussian function $\text{cor}^s(d, 0)$ again. The function $\text{cor}^s(d, 0)$ measured experimentally can be expressed very well using a Gaussian function.

Under these conditions, we obtain a single connection between the apparent and the true correlation function and, correspondingly, between L_θ^s and L_θ^w.

$$\exp\left(-\left(\frac{d}{L_\theta^s}\right)^2\right) = \exp\left(-\frac{d^2}{2s^2 + (L_\theta^w)^2}\right), \qquad (B.6)$$

$$L_\theta^s = \sqrt{2s^2 + (L_\theta^w)^2}. \qquad (B.7)$$

The apparent correlation length as a function of the true correlation length is presented in figure 26. If the true correlation length is less than 5 mm, the influence of folding is very large. The apparent correlation length, L_θ^s, is a factor of 2 larger at $L_\theta^w = 5$ mm. The measured correlation lengths are typically around 15 mm. This corresponds to a true correlation length of ≈ 12.5 mm. The maximal deviation amounts in our case to 20%.

References

[1] Zweben S J and Gould R W 1985 *Nucl. Fusion* **25** 171

[2] Wooton A J, Carreras B A, Matsumoto H, McGuire K, Peebles W A, Ritz C P, Terry P W and Zweben S J 1990 *Phys. Fluids* B **2** 2879

[3] Carreras B A 1997 *IEEE Trans. Plasma Sci.* **25** 1281

[4] Endler M 1999 *J. Nucl. Mater.* **266–269** 84

[5] Ritz Ch P, Powers E J, Rhodes T L, Bengtson R D, Gentle K W, Hong Lin, Phillips P E and Wootton A J 1988 *Rev. Sci. Instrum.* **59** 1739

[6] Bleuel J *et al* 1996 *Proc. 23rd Eur. Conf. on Controlled Fusion and Plasma Physics (Kiev, Ukraine)* vol 20C (Kiev: European Physical Society) part 2, p 727

[7] Zoletnik S, Fiedler S, Kocsis G, McCormick G K, Schweinzer J and Winter H P 1998 *Plasma Phys. Control. Fusion* **40** 1399

[8] Rogers B N, Drake J F and Zeiler A 1998 *Phys. Rev. Lett.* **81** 4396

[9] Xu X Q, Cohen R H, Rognlien T D and Myra J R 2000 *Phys. Plasmas* **7** 1951

[10] Jenko F and Scott B D 1999 *Phys. Plasmas* **6** 2705

[11] Hallatschek K and Zeiler A 2000 *Phys. Plasmas* **7** 2554

[12] McKee G R, Ashley R, Durst R, Fonck R, Jakubowski M, Tritz K, Burrell K, Greenfield C and Robinson J 1999 *Rev. Sci. Instrum.* **70** 913

[13] Zweben S J *et al* 2002 *Phys. Plasmas* **9** 1981

[14] Griem H R 1964 *Plasma Spectroscopy* (New York: McGraw-Hill)

[15] Huber A 1997 *PhD Thesis Report* Jül-3422 ISSN 0944-2952, Institut für Plasmaphysik, Jülich

[16] Pospieszczyk A *et al* 1989 *J. Nucl. Mater.* **162–164** 574

[17] Kadota K, Matsunaga K, Igushi H, Fujiwara M, Tsuchida K and Fujita J 1982 *J. Appl. Phys.* **21** L260

[18] Lie Y T, Höthker K, Bieger W and Kadota K 1984 *Proc. Int. Conf. on Plasma Physics (Lausanne, Switzerland)* vol II, p 320

[19] Schweer B 1993 *Workshop on the Use of Atomic Beams in Plasma Experiments (Budapest, Hungary) KFKI–1993–19/D Report* p 103

[20] Janev R K, Smith J J, Aumayr F, Wutte D, Schneider M, Winter H P and Schweinzer J 1993 Atomic collision database for Li beam interaction with fusion plasmas *IAEA Report* INDC(NDS)-267

[21] Aumayr F and Winter H 1987 Atomic data base for lithium beam-activated plasma diagnostics *IAP-Report* 1/87

[22] Schweinzer J, Wutte D and Winter H 1994 *J. Phys. B: At. Mol. Opt. Phys.* **27** 137

[23] Fiedler S 1994 *PhD Thesis* Technische Universität *Wien Report* IPP III/209, Max-Planck Institut für Plasmaphysik, Garching

[24] Wiese W L, Smith M W and Glennon B M 1966 *Atomic Transition Probabilities, vol I: Hydrogen Through Neon* (Washington: US Government Printing Office) NSRDS-NBS 4

[25] Rudyj A, Carlson A, Endler M, Giannone L, Niedermeyer H, Theimer G and the ASDEX-Team 1990 *Proc. 17th Eur. Conf. on Controlled Fusion and Plasma Heating (Amsterdam, Holland)* vol 14B (Amsterdam: European Physical Society) part III, p 1464

[26] Niedermeyer H, Carlson A, Endler M, Giannone L, Rudyj A, Theimer G and the ASDEX-Team 1991 *Proc. 18th Eur. Conf. on Controlled Fusion and Plasma Physics (Berlin, Germany)* vol 15C (Berlin: European Physical Society) part 1, p 301

[27] Thiel M 1988 *Diploma Work* Fachhochschule Aachen

[28] Bogen P and Hintz E 1984 Plasma edge diagnostics using optical methods *Proc. NATO Advanced Study Institute Entitled Physics of Plasma–Wall Interactions in Controlled Fusion (Quebec, Canada)* (*NATO ASI Series B: Physics* vol 131) p 211

[29] Bracewell R N 1986 *The Fourier Transform and its Applications* (New York: McGraw-Hill)

[30] Coda S and Porkolab M 1997 *Proc. 24th Eur. Conf. on Controlled Fusion and Plasma Physics (Berchtesgaden, Germany)* vol 21A (Berchtesgaden: European Physical Society) part III, p 1141

[31] Nedospasov A V 1992 *J. Nucl. Mater.* **196–198** 90

[32] Berk H L *et al* 1993 *Nucl. Fusion* **33** 263

[33] Xu X Q 1993 *Phys. Fluids* B **5** 3641

[34] Cohen R N 1994 *Contrib. Plasma Phys.* **34** 232

[35] Samm U *et al* 1996 *Plasma Phys. Rep.* **22** 607

[36] Nedospasov A V 1996 *Contrib. Plasma Phys.* **36** 197

[37] Huber A, Nedospasov A V, Samm U and Schweer B 1999 *J. Nucl. Mater.* **266–269** 546

[38] Beall J M, Kim Y C and Powers E J 1982 *J. Appl. Phys.* **53** 3933

[39] Carlson A, Rudyj A and the ASDEX-Team 1990 *Proc. 17th Eur. Conf. on Controlled Fusion and Plasma Heating (Amsterdam, Holland)* vol 14B (Amsterdam: European Physical Society) part IV, p 1676

[40] Carlson A W 1991 *J. Appl. Phys.* **70** 4033

[41] Terry J L *et al* 2003 *Phys. Plasmas* **10** 1739

[42] Bleuel J, Endler M, Niedermeyer H, Schubert M, Thomsen H and the W7-AS Team 2002 *New J. Phys.* **4** 38.1

[43] Endler M, Niedermeyer H, Giannone L, Holzauer E, Rudyj A, Theimer G, Tsois N and the ASDEX Team 1995 *J. Nucl. Mater.* **35** 1307